

Anisotropic magnetohydrodynamic turbulence driven by parametric decay instability: the onset of phase mixing and Alfvén wave turbulence

MUNEHITO SHODA¹ AND TAKAAKI YOKOYAMA¹

¹*Department of Earth and Planetary Science, The University of Tokyo, Hongo, Bunkyo-ku, Tokyo, 113-0033, Japan*

ABSTRACT

We conduct a three-dimensional magnetohydrodynamic (MHD) simulation of the parametric decay instability of Alfvén waves and resultant compressible MHD turbulence, which is likely to develop in the solar wind acceleration region. Because of the presence of the mean magnetic field, the nonlinear stage is characterized by filament-like structuring and anisotropic cascading. By calculating the timescales of phase mixing and the evolution of Alfvén wave turbulence, we have found that the early nonlinear stage is dominated by phase mixing, while the later phase is dominated by imbalanced Alfvén wave turbulence. Our results indicate that the regions in the solar atmosphere with large density fluctuation, such as the coronal bottom and wind acceleration region, are heated by phase-mixed Alfvén waves, while the other regions are heated by Alfvén wave turbulence.

Keywords: magnetohydrodynamics (MHD) – methods: numerical – turbulence – waves

1. INTRODUCTION

Since the discovery of the high-temperature solar atmosphere and supersonic outflow from the Sun, coronal heating and solar wind acceleration have become one of the most important research subjects in astrophysics. *Parker Solar Probe* (Fox et al. 2016) is going to be launched to resolve these long-standing problems in solar physics.

In the open field regions, the wave/turbulence model is promising as the heating mechanism (Cranmer 2012). Several photospheric observations have shown that transverse waves have sufficient energy flux at the photosphere (Fujimura & Tsuneta 2009; Chitta et al. 2012), and a certain portion of these waves propagates through the chromosphere into the corona to power the solar wind (De Pontieu et al. 2007; McIntosh et al. 2011). Non-thermal coronal line broadening (Banerjee et al. 2009; Hahn & Savin 2013) also indicates sufficiently strong Alfvén waves in the corona.

While the global energetics of the corona and solar wind is clarified by wave observations, the energy cascading mechanism is still under investigation. We note that, because there is a large gap between the energy-containing scale and the dissipation scale of Alfvén

waves in the corona and solar wind, the cascading rate gives the approximate plasma heating rate. There are mainly three promising cascading mechanisms: Alfvén wave turbulence (AWT) (Dobrowolny et al. 1980; Perez & Chandran 2013), phase mixing (PM) (Heyvaerts & Priest 1983; Magyar et al. 2017), and parametric decay instability (PDI) (Suzuki & Inutsuka 2005; Tenerani & Velli 2013).

AWT is triggered by counter-propagating Alfvén waves (Kraichnan 1965; Goldreich & Sridhar 1995). In the corona and solar wind, partial reflection due to the field-aligned gradient of Alfvén speed (Velli 1993; Verdini & Velli 2007) can drive AWT. Some theoretical models reproduce the corona and solar wind self-consistently based on the AWT heating scenario (Cranmer et al. 2007; Verdini et al. 2010; Chandran et al. 2011). However, recent three-dimensional simulations indicate that the heating by AWT is insufficient (Perez & Chandran 2013; van Ballegoijen & Asgari-Targhi 2017).

PM works when the Alfvén speed is inhomogeneous in the direction perpendicular to the mean magnetic field (Heyvaerts & Priest 1983). Since the horizontal density variation is observed in the corona (Raymond et al. 2014), PM plays a role in the coronal heating. In fact, a similar process called resonant absorption is observed to work in the solar atmosphere (Okamoto et al. 2015). A recent magnetohydrodynamic simulation has shown that

PM can generate a turbulent structure, and this process is called generalized phase mixing (Magyar et al. 2017).

PDI is an instability of the Alfvén wave (Sagdeev & Galeev 1969; Goldstein 1978), in which an Alfvén wave decays into a forward slow-mode wave and backward Alfvén wave in a low-beta regime. PDI can be a source of coronal heating because slow shocks are generated, heating up the corona and solar wind (Suzuki & Inutsuka 2005; Shoda et al. 2018a). Several processes in the solar wind are possibly attributable to PDI, such as the cross helicity evolution (Malara et al. 2000; Shoda & Yokoyama 2016), density fluctuation (Bowen et al. 2018; Shoda et al. 2018b), and power spectrum formation (Chandran 2018). Both numerical simulation (Suzuki & Inutsuka 2005; Shoda et al. 2018a) and radio-wave observation (Miyamoto et al. 2014) show large density fluctuations in the wind acceleration region, possibly generated by PDI. These results indicate that the plasmas in that region are in a state of PDI-driven turbulence.

In this study, we conduct a simulation of PDI-driven turbulence to clarify which of the process mentioned above is the most responsible for energy cascading (and dissipation). Multi-dimensional simulations of PDI-driven turbulence have already been performed, focusing mainly on the spectral property (Ghosh & Goldstein 1994) or the dependence on dimensions (Del Zanna et al. 2001), although no simulations have ever been performed focusing on the cascading process. We perform a detailed analysis to reveal the dominant process in each phase of instability and turbulence.

2. METHOD

2.1. Basic equations and solver

We numerically solve the ideal MHD equations:

$$\frac{\partial}{\partial t} \rho + \nabla \cdot (\rho \mathbf{v}) = 0, \quad (1)$$

$$\frac{\partial}{\partial t} (\rho \mathbf{v}) + \nabla \cdot \left(p_T \hat{\mathbf{I}} + \rho \mathbf{v} \mathbf{v} - \frac{1}{4\pi} \mathbf{B} \mathbf{B} \right) = 0, \quad (2)$$

$$\frac{\partial}{\partial t} \mathbf{B} + \nabla \cdot (\mathbf{v} \mathbf{B} - \mathbf{B} \mathbf{v}) = 0, \quad (3)$$

$$\frac{\partial}{\partial t} e + \nabla \cdot \left[(e + p_T) \mathbf{v} - \frac{1}{4\pi} \mathbf{B} (\mathbf{v} \cdot \mathbf{B}) \right] = 0, \quad (4)$$

$$e = \frac{p}{\Gamma - 1} + \frac{1}{2} \rho \mathbf{v}^2 + \frac{\mathbf{B}^2}{8\pi}, \quad p_T = p + \frac{\mathbf{B}^2}{8\pi}. \quad (5)$$

$\Gamma = 1.0001$ is used instead of the adiabatic value $\Gamma = 5/3$ to keep the system almost isothermal. Since we are interested in the cascading process, we exclude the diffusion terms; mechanical energy is thermalized by numerical diffusion at the grid scale.

The HLLD Riemann solver (Miyoshi & Kusano 2005) with WENOZ reconstruction (Borges et al. 2008) and SSP Runge-Kutta method (Shu & Osher 1988) are used for numerical calculation. This is a high-resolution (5th-order-in-space and 3rd-order-in-time) shock-capturing numerical scheme, which is appropriate for the simulation of PDI. Numerical $\nabla \cdot \mathbf{B}$ error is removed with the hyperbolic cleaning method (Dedner et al. 2002).

2.2. Numerical setup

We solve the basic equations (1)-(5) in a rectangular simulation box $[0, L] \times [0, L] \times [0, 3L]$. We apply $288 \times 288 \times 864$ grid points to resolve the computational domain, so that the grid size is isotropic. The periodic boundary conditions are used for all the boundaries. The initial condition is as follows:

$$\rho = \rho_0 + \delta \rho_0, \quad p = c_s^2 \rho_0, \quad (6)$$

$$v_x = \eta v_{A0} \sin(k_0 z - \omega_0 t), \quad B_x = -B_0 v_x / v_{A0} \quad (7)$$

$$v_y = \eta v_{A0} \cos(k_0 z - \omega_0 t), \quad B_y = -B_0 v_y / v_{A0} \quad (8)$$

$$v_z = 0, \quad B_z = B_0. \quad (9)$$

Note that the box-averaged density, momentum, magnetic field, and total energy are time-independent because of the periodic boundary. $k_0 = 2\pi/L$ and $\omega_0 = v_{A0} k_0$ are the wave number and frequency of the initial wave, respectively. The parent wave period is therefore given as $\tau_0 = 2\pi/\omega_0 = L/v_{A0}$. c_s and $v_{A0} = B_0/\sqrt{4\pi\rho_0}$ denote the background sound and Alfvén velocities, respectively. η is the normalized amplitude of the initial wave. In this study, we fix $\eta = 0.2$ and $c_s/v_{A0} = 0.2$.

The density fluctuation is imposed to trigger PDI. We calculated two cases: three-dimensional (3D) setting and one-dimensional (1D) setting. In the 3D setting, the fluctuations are given as

$$\delta \rho_0 / \rho_0 = \varepsilon \sin(k_0 x) \sin(k_0 y) N(z), \quad (10)$$

where $\varepsilon \sim 10^{-3}$ is the initial amplitude of density fluctuation and $N(z)$ denotes a random noise function of z . The 1D setting is defined as

$$\delta \rho_0 / \rho_0 = \frac{1}{2} \varepsilon N(z). \quad (11)$$

The factor 1/2 is to make the root-mean-square (rms) value of $\delta \rho_0$ the same as that in the 3D setting.

3. VOLUME-AVERAGED QUANTITIES

First, we discuss the time evolution of volume-averaged characteristic quantities: the normalized rms density fluctuation $\delta \rho_{\text{rms}}/\rho_0$, rms angle between current and magnetic field $\phi_{j,B}$, Elsässer energies E^\pm and

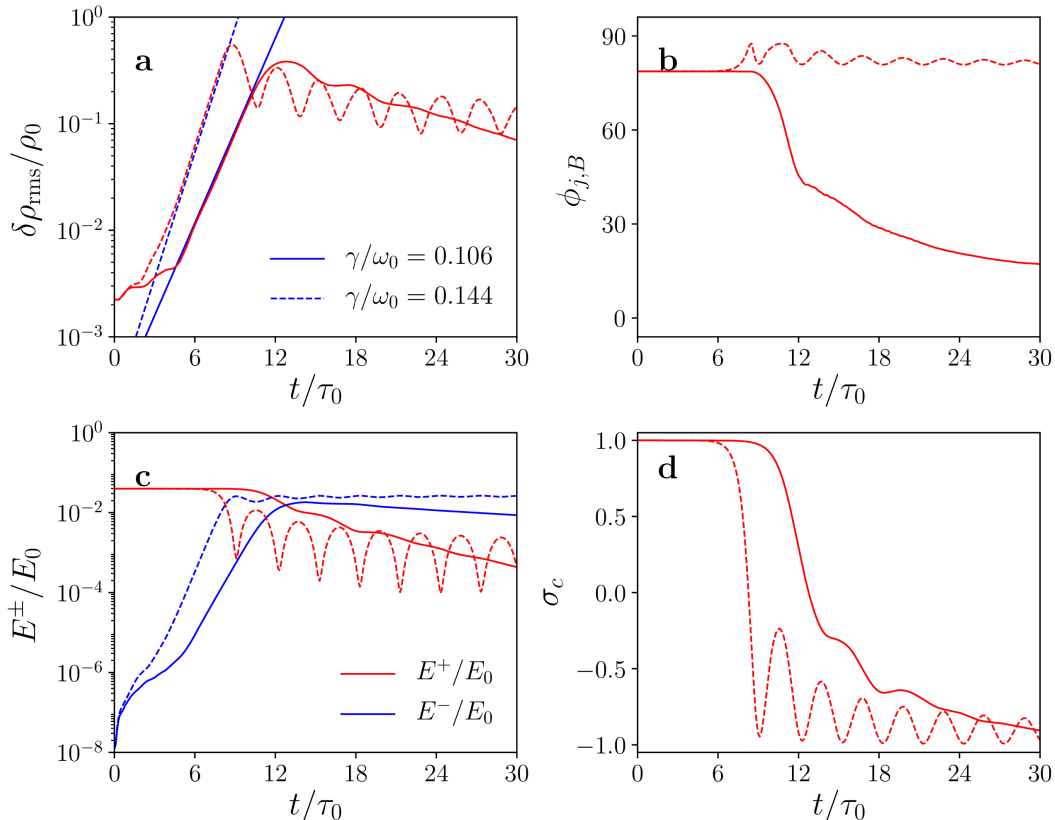


Figure 1. Time evolution of the volume-averaged variables in three-dimensional setting (solid lines) and one-dimensional setting (dashed lines). The horizontal axis (time) is normalized by the period of the parent wave τ_0 . Panels indicate the a: normalized root-mean-square density fluctuation $\delta\rho_{\text{rms}}/\rho_0$, b: angle between current density and magnetic field $\phi_{j,B}$, c: normalized Elsässer energies (red: E^+/E_0 , blue: E^-/E_0), and d: normalized cross helicity σ_c , respectively. The blue lines in Panel a are the exponential fitting $\delta\rho_{\text{rms}} \propto \exp(\gamma t)$ in the linear growth stage.

normalized cross helicity σ_c . $\delta\rho_{\text{rms}}$ is defined as

$$\delta\rho_{\text{rms}} = \sqrt{\langle(\rho - \rho_0)^2\rangle} = (\rho - \rho_0)_{\text{rms}}, \quad (12)$$

where $\langle X \rangle$ and X_{rms} denote the volume-average and rms operators, respectively:

$$\langle X \rangle = \frac{1}{V} \int d\mathbf{x} X, \quad X_{\text{rms}} = \sqrt{\frac{1}{V} \int d\mathbf{x} X^2}, \quad (13)$$

where $V = 3L^3$ denotes the volume of the simulation box. $\phi_{j,B}$ is given by

$$\phi_{j,B} = \left[\arccos^{-1} \left(\frac{\mathbf{j} \cdot \mathbf{B}}{|\mathbf{j}| |\mathbf{B}|} \right) \right]_{\text{rms}}, \quad (14)$$

where

$$\mathbf{j} = \frac{c}{4\pi} \nabla \times \mathbf{B}. \quad (15)$$

Normalized Elsässer energies are defined as:

$$E^\pm = \langle \frac{1}{4} \rho \zeta^{\pm 2} \rangle / E_0, \quad (16)$$

where $E_0 = \rho_0 v_{A0}^2$ and $\zeta^\pm = \mathbf{v}_\perp \mp \mathbf{B}_\perp / \sqrt{4\pi\rho}$ are Elsässer variables (Elsässer 1950). The subscript \perp denotes the components perpendicular to the mean field $B_0 \mathbf{e}_z$. The normalized cross helicity σ_c is calculated from E^\pm as (Del Zanna et al. 2001)

$$\sigma_c = \frac{E^+ - E^-}{E^+ + E^-}. \quad (17)$$

In Figure 1, we show the time evolution of the volume-averaged quantities defined above by solid lines. The corresponding values calculated with the 1D setting are also shown by dashed lines in each panel. The blue lines in Figure 1a are fitted lines that give the growth rates γ in the linear phase.

Figure 1a shows that the 3D growth rate ($\gamma/\omega_0 = 0.106$) is 26% smaller than the 1D growth rate ($\gamma/\omega_0 = 0.144$). This indicates that the 3D structure of density fluctuation works to reduce the growth rate of PDI. Note that both values are smaller than the analytical value ($\gamma/\omega_0 = 0.157$) by Goldstein (1978). $\delta\rho_{\text{rms}}/\rho_0$ in the 1D calculation shows an oscillation that is anti-correlated

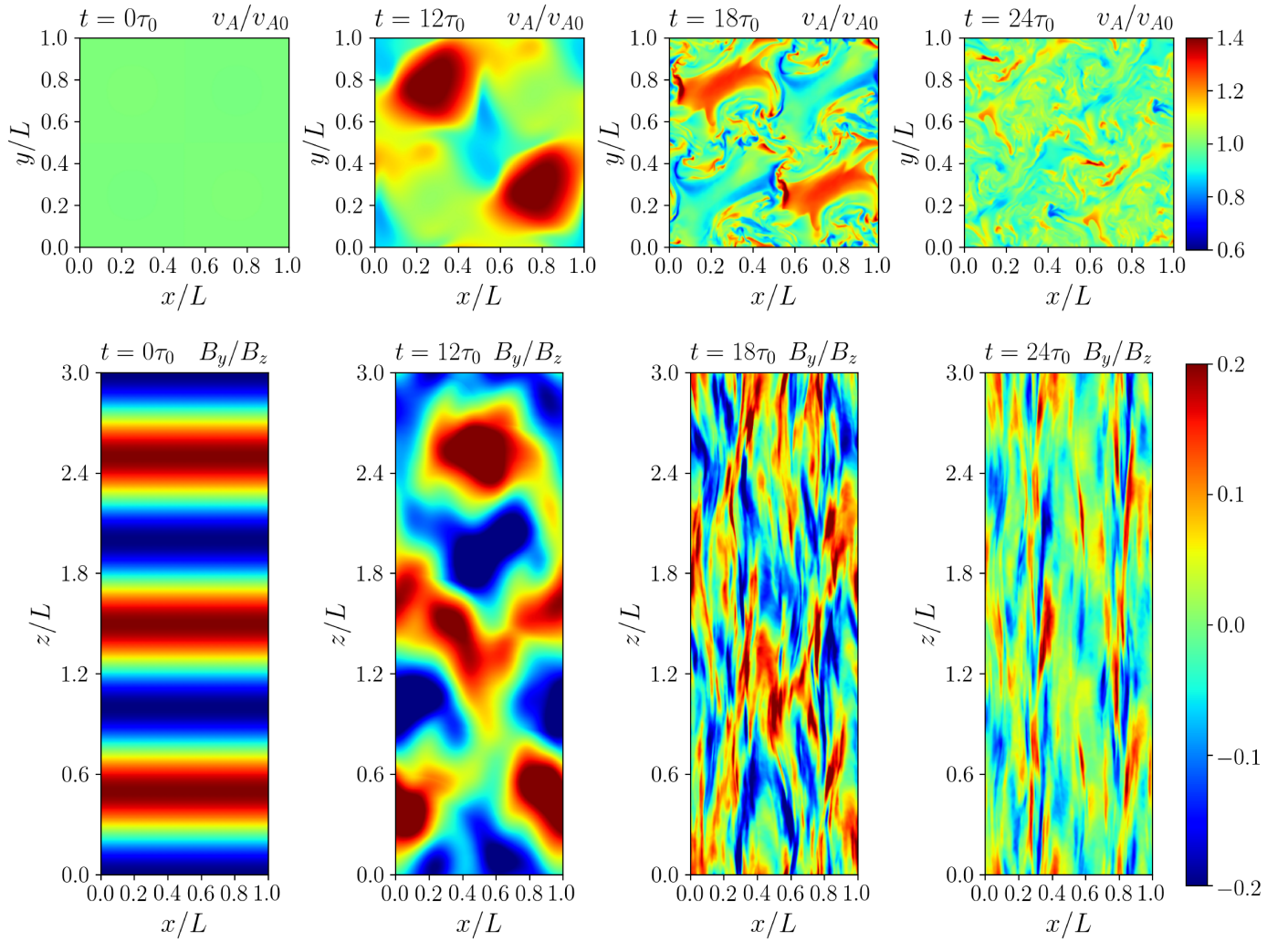


Figure 2. Snapshots of the normalized Alfvén speed v_A/v_{A0} on the xy plane ($z = 0$, upper panels) and normalized amplitude of Alfvén wave B_y/B_z on the xz plane ($y = 0$, lower panels). From left to right, the snapshots shown are $t = 0$ (initial condition), $t = 12\tau_0$ (saturation phase), $t = 18\tau_0$ (early nonlinear phase), and $t = 24\tau_0$ (fully nonlinear phase). (An animation of this figure is available.)

with E^+ (Figure 1a, 1c). This is a resonant energy exchange between forward Alfvén and sound waves (Shoda & Yokoyama 2016).

Figure 1b shows that the alignment between \mathbf{j} and \mathbf{B} occurs because of turbulence. This is sometimes called selective decay (Biskamp 2003); the magnetic field approaches force-free field turbulence. $\phi_{j,B}$ cannot be 0 because the system has a finite cross helicity (Stribling & Matthaeus 1991).

From Figure 1c, we can tell the energy dissipation rate of Alfvén waves. In the later phase of 1D calculation, E^- is almost constant because there exists no significant physical mechanism that dissipates backward Alfvén waves. Meanwhile, in the nonlinear phase of 3D calculation, both E^+ and E^- decreases with time, and

the larger component has the smaller decay rate. This is the behavior of dynamic alignment (Dobrowolny et al. 1980; Biskamp 2003); the minor Elsässer variable decays faster.

4. ANISOTROPIC BEHAVIOR OF TURBULENCE

Next, we discuss the structure of turbulence on 2D planes. Figure 2 shows the spatial distributions of the normalized Alfvén speed v_A/v_{A0} (where $v_A = B_z/\sqrt{4\pi\rho}$) on the xy plane (upper panels) and the normalized amplitude B_y/B_z on the xz plane (lower panels) of different t : from left to right $t = 0$ (initial condition), $t = 12\tau_0$ (saturation phase), $t = 18\tau_0$ (early nonlinear phase), and $t = 24\tau_0$ (fully nonlinear phase). The inhomogeneity in the upper panel is the trigger of

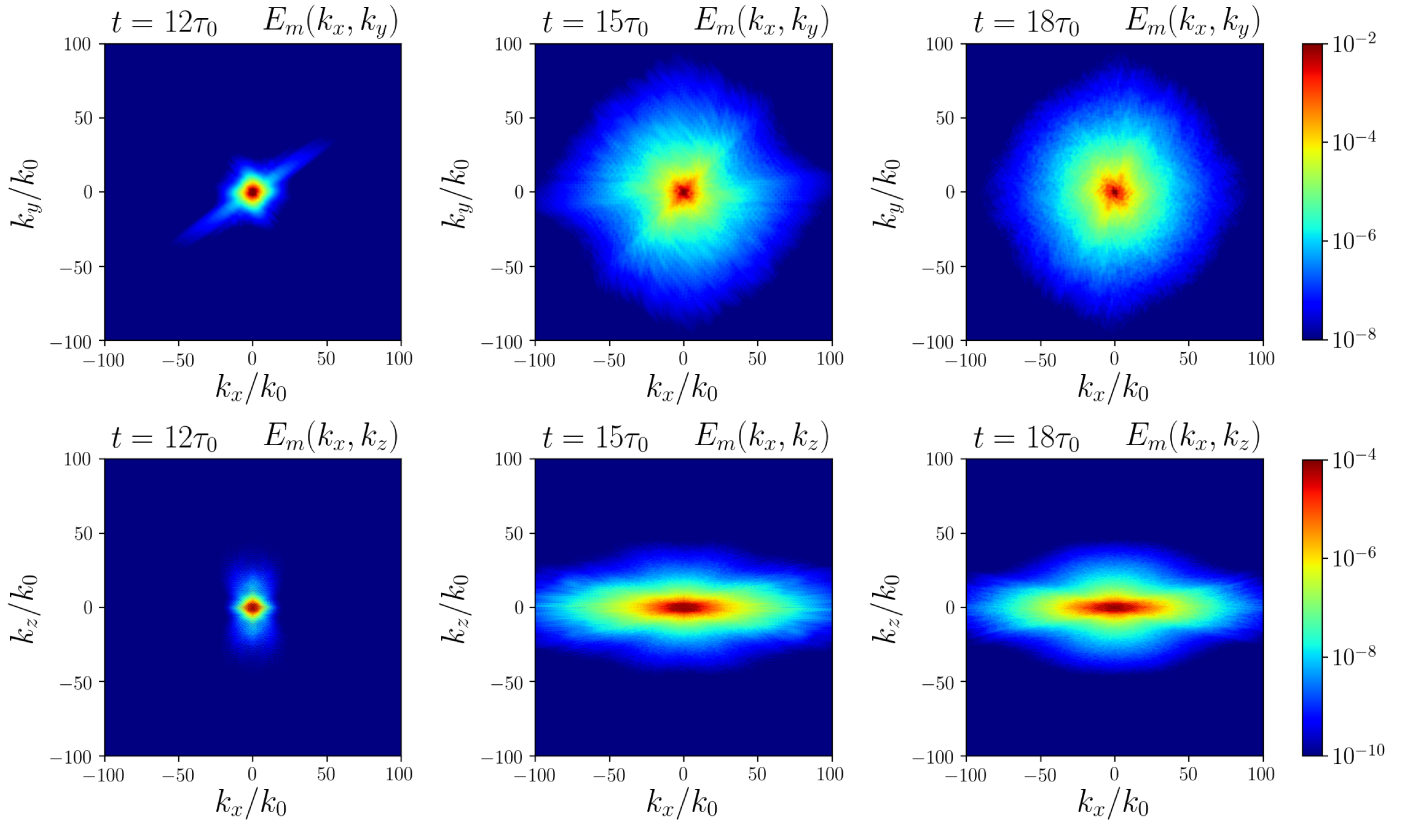


Figure 3. Normalized two-dimensional magnetic energy spectra in the xy directions ($E_m(k_x, k_y)$, upper panels) and in the xz directions ($E_m(k_x, k_z)$, lower panels) from the saturation to nonlinear phase. The corresponding times are $t = 12/\tau_0$ (left), $t = 15\tau_0$ (middle), and $t = 18\tau_0$ (right), respectively.

PM, while the filament-like structure is observed in the lower panels because of PM.

As time proceeds, the structure of B_y/B_z becomes aligned with the mean magnetic field $B_0\mathbf{e}_z$; the phase structure becomes progressively finer in the direction perpendicular to the mean field. Both PM and AWT can generate these structures, and therefore, we cannot distinguish them here. PM certainly works in the nonlinear phase because there exists a perpendicular gradient of v_A (upper panels in Figure 2); AWT also works because there are bidirectional Alfvén waves and the dynamic alignment is observed (Figure 1c 1d). In Section 5, we discuss the dominances of PM and AWT.

Anisotropy also appears in the energy spectrum. To observe the time evolution of anisotropy, we calculate the normalized magnetic energy spectrum E_m with different times. Specifically, we concentrate on the 2D spectrum in the xy directions and xz directions aver-

aged over the other direction, defined as

$$E_m(k_x, k_y) = \frac{\Delta k_x \Delta k_y}{3L} \int dz \frac{\mathbf{B}(k_x, k_y, z)^2}{B_0^2}, \quad (18)$$

$$E_m(k_x, k_z) = \frac{\Delta k_x \Delta k_z}{L} \int dy \frac{\mathbf{B}(k_x, y, k_z)^2}{B_0^2}, \quad (19)$$

$$\Delta k_x = \Delta k_y = \frac{2\pi}{L}, \quad \Delta k_z = \frac{2\pi}{3L} \quad (20)$$

where, for example, $\mathbf{B}(k_x, y, z)$ denotes the Fourier transformation of $\mathbf{B}(x, y, z)$ with respect to x .

Figure 3 shows $E_m(k_x, k_y)$ (upper panels) and $E_m(k_x, k_z)$ (lower panels) at $t = 12\tau_0$ (left), $t = 15\tau_0$ (middle), and $t = 18\tau_0$ (right), respectively. The upper panels show isotropic behavior, indicating that the turbulence is axisymmetric with respect to the mean magnetic field. In contrast, the lower panels show anisotropic distributions; the contour is elongated along k_x in the nonlinear phase. This elongation shows that the cascading proceeds faster in the perpendicular (x) direction than in the parallel (z) direction, which is consistent with the classical theory of AWT (Goldreich & Sridhar 1995). In fact, the typical aspect ratio (k_z/k_x)

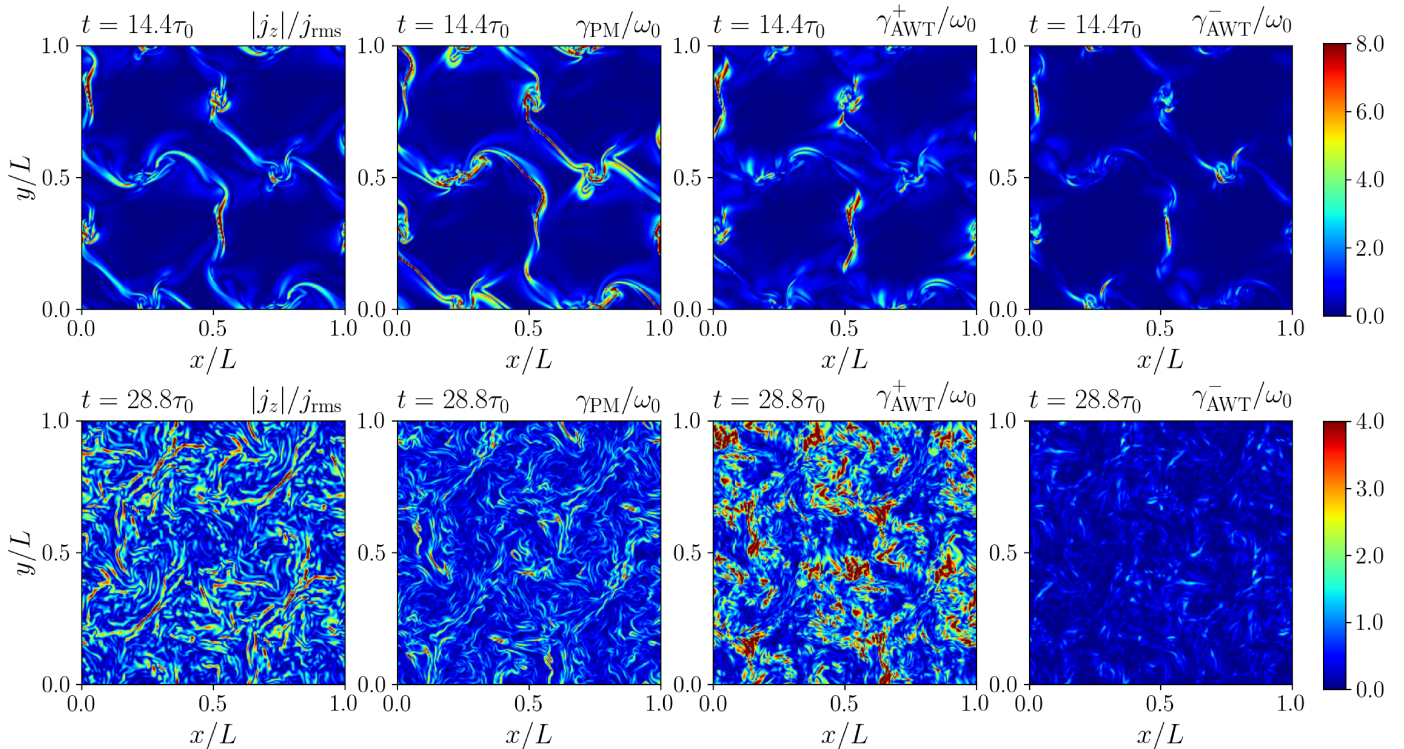


Figure 4. Snapshots of the spatial distributions of $2|j_z|/j_{\text{rms}}$ (left), $\gamma_{\text{PM}}/\omega_0$ (middle-left), $\gamma_{\text{AWT}}^+/\omega_0$ (middle-right), and $\gamma_{\text{AWT}}^-/\omega_0$ (right). The upper and lower panels correspond to the early nonlinear phase $t = 14.4\tau_0$ and the late nonlinear phase $t = 28.8\tau_0$, respectively.

of the spectrum is approximately the same as the nonlinearity ($\delta v/v_A$), and this indicates the critical balance of AWT (Goldreich & Sridhar 1995).

5. PHASE MIXING VERSUS ALFVÉN WAVE TURBULENCE

Both PM (phase mixing) and AWT (Alfvén wave turbulence) yield anisotropy, and this similarity makes it difficult to distinguish the physical processes. Here, by calculating the timescale of each process, we aim to clarify which process is dominant in a certain phase.

To estimate the timescale of PM and AWT, we derive the analytical expression of the timescale of PM and AWT. Because both processes are caused by Alfvén waves, reduced MHD (RMHD) approximation is convenient. In the absence of parallel flow and parallel gradients of density and magnetic field, the Alfvén wave propagation is described as follows (Verdini & Velli 2007):

$$[\partial/\partial t \pm v_{A\parallel} \nabla_{\parallel}] \zeta^{\pm} = -(\zeta^{\mp} \cdot \nabla_{\perp}) \zeta^{\pm}, \quad (21)$$

where

$$\nabla_{\parallel} = e_z \frac{\partial}{\partial z}, \quad \nabla_{\perp} = e_x \frac{\partial}{\partial x} + e_y \frac{\partial}{\partial y}. \quad (22)$$

The second term on the left hand side is the term for propagation and PM, while the first term on the right

hand side corresponds to AWT. Even though the RMHD approximation does not hold in our simulation, Eq. (21) approximately describes the Alfvén wave propagation and provides a general understanding of the physical process that is not related to compressibility.

We begin by deriving the timescale of PM. Nonlinear terms are ignored here because PM is a linear process triggered by the perpendicular variance of the Alfvén speed. Taking the perpendicular rotation ($\nabla_{\perp} \times$) of Eq. (21), we obtain

$$[\partial/\partial t \pm v_{A\parallel} \nabla_{\parallel}] (\nabla_{\perp} \times \zeta^{\pm}) = \mp (\nabla_{\perp} v_{A\parallel}) \times \frac{\partial}{\partial z} \zeta^{\pm}. \quad (23)$$

The right-hand-side term represents the phase mixing. From this equation, the growth rate of PM (γ_{PM}) is approximately given as follows:

$$\gamma_{\text{PM}} \approx |\nabla_{\perp} v_{A\parallel}|. \quad (24)$$

Next, we calculate the timescale of AWT. Ignoring the linear term in Eq. (21), the decay rate of Alfvén wave turbulence is given as

$$\gamma_{\text{AWT}}^{\pm} \approx \frac{|(\zeta^{\mp} \cdot \nabla_{\perp}) \zeta^{\pm}|}{\langle \zeta^{\pm} \rangle_{\text{rms}}}, \quad (25)$$

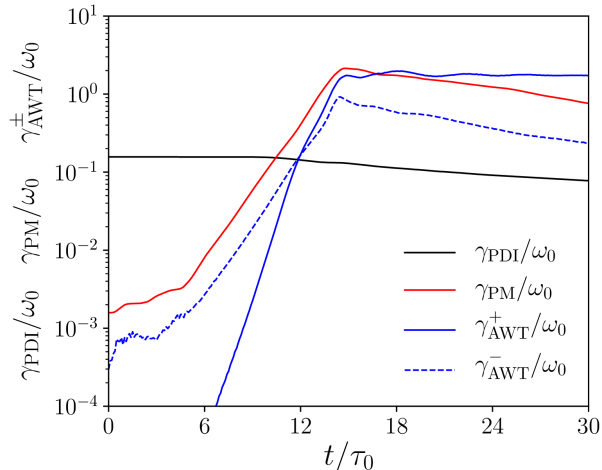


Figure 5. Time evolution of rms timescales of phase mixing γ_{PM} (red solid), Alfvén wave turbulence of forward propagating mode γ_{AWT}^+ (blue solid) and backward propagating mode γ_{AWT}^- (blue dashed), and parametric decay instability γ_{PDI} normalized by the initial-wave angular frequency ω_0 .

where $\tilde{\zeta}^\mp$ denote the fluctuating parts of Elsässer variables:

$$\tilde{\zeta}^\mp = \zeta^\mp - \frac{1}{L^2} \int dx dy \zeta^\mp. \quad (26)$$

We evaluate the nonlinear operator as $\tilde{\zeta}^\mp \cdot \nabla_\perp$ instead of $\zeta^\mp \cdot \nabla_\perp$ because the perpendicularly uniform mode does not contribute to the wave distortion (energy cascading).

In Figure 4, we show the spatial distribution of j_z/j_{rms} , γ_{PM} and γ_{AWT}^\pm on the xy plane in an early nonlinear phase ($t = 14.4\tau_0$, upper panels) and a late nonlinear phase ($t = 28.8\tau_0$, lower panels). Note that j_z/j_{rms} indicates the degree of development of the perpendicular cascading. In an early phase, γ_{PM} is larger than γ_{AWT}^\pm and it is spatially correlated with j_z/j_{rms} and γ_{AWT}^\pm . This shows that the early nonlinear phase is dominated by PM-driven turbulence (Magyar et al.

2017). In the later phase, the magnitude relation is reversed; γ_{AWT}^+ becomes the largest and this indicates that the later phase is characterized by Alfvén wave turbulence. Specifically, AWT in the later phase is imbalanced ($E^+ \ll E^-$, Figure 1c), and thus the dynamic alignment proceeds (Figure 1d).

Figure 5 shows the rms values of γ_{PM} (red solid line), γ_{AWT}^+ (blue solid line), and γ_{AWT}^- (blue dashed line) versus time. In addition to these, we also calculate the normalized growth rate of PDI (γ_{PDI}) from the dispersion relation given by Goldstein (1978) and show its time evolution with a black line.

Figure 5 gives some important indications. First, the system is dominated by different processes, depending on the phase. The initial phase ($0 \leq t/\tau_0 \lesssim 8$) is dominated by the growth of PDI because γ_{PDI} is the largest. Before the saturation to early nonlinear phase ($8 \lesssim t/\tau_0 \lesssim 16$), PM becomes active because of the large density fluctuation (Figure 1a). Finally, in the fully nonlinear phase ($16 \lesssim t/\tau_0$), the system is characterized by imbalanced ($\gamma_{\text{AWT}}^+ \gg \gamma_{\text{AWT}}^-$) AWT.

Second, because the timescale of γ_{PM} is clearly correlated with $\delta\rho_{\text{rms}}/\rho_0$, PM should be of importance in the large-density-fluctuation regions. In the corona and solar wind, such a region is either the coronal bottom (Raymond et al. 2014) or the wind acceleration region (Miyamoto et al. 2014). Specifically, the fast saturation of nonthermal line broadening in the corona (Hahn & Savin 2013) possibly comes from PM because of the presence of large density fluctuations near the coronal bottom (Raymond et al. 2014).

M.S. is supported by the Leading Graduate Course for Frontiers of Mathematical Sciences and Physics (FMSP) and Grant-in-Aid for Japan Society for the Promotion of Science (JSPS) Fellows. T.Y. is supported by JSPS KAKENHI Grant Number 15H03640. Numerical computations were carried out on Cray XC30 at Center for Computational Astrophysics, National Astronomical Observatory of Japan.

REFERENCES

- Banerjee, D., Pérez-Suárez, D., & Doyle, J. G. 2009, *A&A*, 501, L15
- Biskamp, D. 2003, *Magnetohydrodynamic Turbulence*, 310
- Borges, R., Carmona, M., Costa, B., & Don, W. S. 2008, *Journal of Computational Physics*, 227, 3191
- Bowen, T. A., Badman, S., Hellinger, P., & Bale, S. D. 2018, *ApJL*, 854, L33
- Chandran, B. D. G. 2018, *Journal of Plasma Physics*, 84, 905840106
- Chandran, B. D. G., Dennis, T. J., Quataert, E., & Bale, S. D. 2011, *ApJ*, 743, 197
- Chitta, L. P., van Ballegoijen, A. A., Rouppe van der Voort, L., DeLuca, E. E., & Kariyappa, R. 2012, *ApJ*, 752, 48
- Cranmer, S. R. 2012, *SSRv*, 172, 145
- Cranmer, S. R., van Ballegoijen, A. A., & Edgar, R. J. 2007, *ApJS*, 171, 520
- De Pontieu, B., et al. 2007, *Science*, 318, 1574

- Dedner, A., Kemm, F., Kröner, D., Munz, C.-D., Schnitzer, T., & Wesenberg, M. 2002, *Journal of Computational Physics*, 175, 645
- Del Zanna, L., Velli, M., & Londrillo, P. 2001, *A&A*, 367, 705
- Dobrowolny, M., Mangeney, A., & Veltri, P. 1980, *Physical Review Letters*, 45, 144
- Elsässer, W. M. 1950, *Physical Review*, 79, 183
- Fox, N. J., et al. 2016, *SSRv*, 204, 7
- Fujimura, D., & Tsuneta, S. 2009, *ApJ*, 702, 1443
- Ghosh, S., & Goldstein, M. L. 1994, *J. Geophys. Res.*, 99, 13
- Goldreich, P., & Sridhar, S. 1995, *ApJ*, 438, 763
- Goldstein, M. L. 1978, *ApJ*, 219, 700
- Hahn, M., & Savin, D. W. 2013, *ApJ*, 776, 78
- Heyvaerts, J., & Priest, E. R. 1983, *A&A*, 117, 220
- Kraichnan, R. H. 1965, *Physics of Fluids*, 8, 1385
- Magyar, N., Van Doorselaere, T., & Goossens, M. 2017, *Scientific Reports*, 7, 14820
- Malara, F., Primavera, L., & Veltri, P. 2000, *Physics of Plasmas*, 7, 2866
- McIntosh, S. W., de Pontieu, B., Carlsson, M., Hansteen, V., Boerner, P., & Goossens, M. 2011, *Nature*, 475, 477
- Miyamoto, M., et al. 2014, *ApJ*, 797, 51
- Miyoshi, T., & Kusano, K. 2005, *Journal of Computational Physics*, 208, 315
- Okamoto, T. J., Antolin, P., De Pontieu, B., Uitenbroek, H., Van Doorselaere, T., & Yokoyama, T. 2015, *ApJ*, 809, 71
- Perez, J. C., & Chandran, B. D. G. 2013, *ApJ*, 776, 124
- Raymond, J. C., McCauley, P. I., Cranmer, S. R., & Downs, C. 2014, *ApJ*, 788, 152
- Sagdeev, R. Z., & Galeev, A. A. 1969, *Nonlinear Plasma Theory*
- Shoda, M., & Yokoyama, T. 2016, *ApJ*, 820, 123
- Shoda, M., Yokoyama, T., & Suzuki, T. K. 2018a, *ApJ*, 853, 190
- . 2018b, *ArXiv e-prints*
- Shu, C.-W., & Osher, S. 1988, *Journal of Computational Physics*, 77, 439
- Stribling, T., & Matthaeus, W. H. 1991, *Physics of Fluids B*, 3, 1848
- Suzuki, T. K., & Inutsuka, S.-i. 2005, *ApJL*, 632, L49
- Tenerani, A., & Velli, M. 2013, *Journal of Geophysical Research (Space Physics)*, 118, 7507
- van Ballegooijen, A. A., & Asgari-Targhi, M. 2017, *ApJ*, 835, 10
- Velli, M. 1993, *A&A*, 270, 304
- Verdini, A., & Velli, M. 2007, *ApJ*, 662, 669
- Verdini, A., Velli, M., Matthaeus, W. H., Oughton, S., & Dmitruk, P. 2010, *ApJL*, 708, L116